Generating Gradient Germanium Nanostructures by Shock-induced Amorphization and Crystallization

S. Zhao[a], B. Kad[a], C.E. Wehrenberg[b] , B.A. Remington[b], E.N. Hahn[a], K.L. More[c], M.A. Meyers[a*]

[a] *University of California, San Diego, La Jolla, CA 92093, USA*

[b] *Lawrence Livermore National Laboratory, Livermore, CA 94550, USA*

[c] *Oak Ridge National Laboratory, Oak Ridge, TN 21005, USA*

Gradient nanostructures attract renewed interest for their potential to obtain superior structural and functional properties in materials. Applying powerful laser-driven shocks (stresses of up to one-third million atmospheres, or 33 Gigapascals) to germanium, here we report a complex gradient nanostructure consisting, near the surface, of nanocrystals with high density of nanotwins. Beyond there, the structure exhibits arrays of amorphous bands which are preceded by planar defects such as stacking faults (partial dislocations). At a lower stress, the surface region of the recovered target is completely amorphous. It is proposed that germanium undergoes amorphization above a threshold stress and that the deformation-generated heat leads to nanocrystallization. These experiments are corroborated by molecular dynamics simulations which show that supersonic partial dislocation bursts play a role in triggering the crystalline-to-amorphous transition.

Keywords: Germanium, semiconductor, amorphization, nanocrystallization, laser shock

Significance Statements: Amorphization and nanocrystallization are two powerful methods to tune the structural and functional properties of materials by altering their microstructure without changing the overall chemistry. Using powerful laser-driven shocks, we demonstrate that amorphization and nanocrystallization can be achieved within a time scale that is considerably shorter than other conventional techniques. Our results provide compelling insights into pressure/shear amorphization and propose a novel route to fabricate gradient semiconducting nanostructures using lasers. Additionally, shear-driven amorphization is demonstrated as deformation mechanism in this extreme regime.

[*]**Corresponding author: Marc A. Meyers Email: mameyers@eng.ucsd.edu**

Amorphous and gradient nanostructures are drawing intense attention due to their superior functional and mechanical properties (1, 2). Since they are thermodynamically metastable, amorphous materials can transform into nanocrystalline ones if appropriate treatments are applied (3). One of the most common methods to achieve amorphization is to quench a liquid at ultrafast cooling-rates, which is extremely difficult for most pure elements (4). Alternatively, it has been shown that application of pressure leads to amorphization of materials whose melting point displays a negative Clapeyron slope ($dT/dP<0$) (5–9); germanium (Ge) falls into this category (10). However, instead of pressure-induced amorphization, numerous studies, under both static (11, 12) and dynamic conditions (13–15), have shown that Ge undergoes polymorphism at elevated pressures. Consequently, amorphization was not unambiguously identified in Ge until Clarke (16) observed the indentation-induced crystalline-to-amorphous transition. More recently, a high speed nanodroplet test also showed surface amorphization of Ge in an extremely localized manner (17).

Despite being widely studied, the underlying microstructural mechanisms of pressure-induced amorphization remain vague. This is due to the notorious brittleness of germanium at room temperature which renders its recovery from pressurization extremely challenging. The deposition of high-power pulsed laser energy onto a mm-scale target generates transient states of extreme stresses that promptly build up and decay rapidly as the pulse propagates. The short duration of the stress pulse preserves the integrity of the target by suppressing the full development of cracks and enables post-shock microstructure characterization. Using this methodology, we have previously reported shock-induced amorphization in silicon (18) and boron carbide (19). Prior to that, Jeanloz et al.(20) discovered this phenomenon in olivine (iron/magnesium silicate) subjected to shock compression. The important, albeit often ignored, role of shear in pressure-

induced phase transition (21, 22) is clearly evidenced by the directional nature of the amorphous bands.

Experiments were performed at the Omega laser facility, using a pulsed laser with a nominal square pulse shape (wavelength=352 nm; laser duration=1 ns). The nominal laser energies were E_{laser}=20 ~100 J, resulting in intensities of 0.2 ~1.1 TW/cm^2. Fig. 1A shows schematically the shock-recovery assembly. The high-density laser energy vaporizes the polystyrene (CH) ablator, which drives a compressive wave that eventually propagates into the [001] monocrystalline Ge target. For the 100 J experiment, the peak shock stress, $\sigma_{33}\approx$33 GPa, can be inferred indirectly from the particle velocity (U_p) measurement by VISAR (velocity interferometer system for any reflector) experiments (Fig. 1B-D) and impedance matching (Fig. 1E), as detailed in the methods of **supporting information**(**SI**). Note that the shock wave decays rapidly when traveling across the sample thickness, as evidenced by the significant drop of particle velocity at the rear surface (Ge/LiF interface) of the target (Fig. 1D). The time dependence of shock-wave propagation and decay of the longitudinal shock stress as function of depth can be simulated by 1-D hydrodynamic simulation, as shown in Fig. S1 of the **SI**.

Transmission electron microscopy (TEM) was used to inspect the post-shock deformation micro and nanostructure. The TEM samples were extracted by focused ion beam cutting from the as-shocked surface and the microstructural hierarchy is displayed in Fig. 2A. Along the direction of shock-wave propagation (left to right), nanocrystalline material can be observed as deep as 3 μm below the shock surface. Statistical analysis (Fig. 2B) shows that the average grain size is 62$\pm$31 nm, whereas much smaller (5~10 nm) grains can be seen towards the end of nanocrystalline regime. In addition, a high density of {111} nanotwins/stacking faults is identified (Fig. 2D, G), further subdividing the nanostructure. As one goes deeper, deformation bands dominate (Fig. 2C)

with an average width (w_{band}) of 25±17 nm and interspacing ($w_{spacing}$) of 124±63 nm. Fourier-transformed diffraction pattern (inset in Fig. 2E) in these regions shows a mixture of halo ring and sharp spots, suggesting that these bands are essentially amorphous with embedded nanocrystals. In another contrast-free band (Fig. 2F), the halo-ring diffraction indicates a complete amorphous structure. These amorphous bands align roughly with {111} slip planes of the diamond-cubic lattice, which is also close to the maximum shear direction. Moreover, profuse stacking faults can be observed at the amorphous/crystalline interface (Fig. 2H), suggesting that these planar defects serve as the precursors to amorphization. Note that most of these bands align parallel to each other, albeit other variants can be observed which tend to intersect and bifurcate, forming a complex network. This is shown in Fig. 2I; thus, the stacking faults and their intersections are the first stage of amorphous band generation, similar to our previous observations in Si *(16, 24).* At a much lower shock stress (E_{laser} =20 J; $\sigma_{33}\approx$13 GPa), the recovered sample shows bulk amorphization close to the shock surface. The TEM sample (Fig. S2 in **SI**) exhibits a completely amorphous state up to 4 μm below the surface without undergoing crystallization.

To better understand the atomistic mechanisms of amorphization, we have also carried out large-scale molecular dynamics (MD) simulations to mimic laser shock experiments. The Tersoff (23) interatomic potential was implemented and executed in the LAMMPS (24) code. MD simulations (Fig. 3A) show that amorphization occurs above a critical particle velocity of 1.2 km/s during compression and that the directional features of the amorphous bands and massive stacking faults/nanotwin formation before the onset of amorphization (Fig. 3B) agree well with the TEM observation; this strongly suggests that these planar faults are the precursors of amorphous banding. Dislocation velocity measurement (Fig. 3G) from MD snapshots (Fig. 3C-F) shows that these stacking faults can travel supersonically prior to the crystalline-to-amorphous transition;

subsequently their speed drops to the transonic regime. It is proposed that supersonic dislocations have a much-reduced ability to relax shear stresses because of stress-field distortion produced by their velocity; an additional effect is that they radiate energy (25). Thus, their speed drops to the subsonic regime after a short excursion. It is also proposed that supersonic dislocations (stacking faults) transport the imposed energy to their surroundings, which helps to trigger amorphization. The pressure dependence of longitudinal (C_L) and transversal (C_T) sound speed are shown in Fig. S4 in **SI** and the ultra-fast nucleation and motion of dislocation/amorphous band can be viewed in the **supplementary video**.

Germanium melts with a reduction in volume and its melting temperature decreases as pressure increases ($dT/dP \approx -35$ K/GPa (26)). Thus, compressive stresses favor amorphization because the disordered phase possesses a smaller specific volume than the original crystalline phase, although the amorphous state is energetically less favorable at ambient pressure. In addition to pressure, the superposed shear stress also facilitates amorphization by inducing large lattice displacements through stacking-fault generation and propagation (18). This is due to the nature of shock waves which generate a uniaxial strain with high amplitude hydrostatic pressure (P) and shear stresses. The P and the maximum shear stress (τ_{max}) are related through the generalized Hooke's law, as detailed in **SI**.

Applying classical nucleation theory one can obtain the pressure and shear-stress dependence of the nucleation barrier, as explained previously by Zhao *et al*.(27),

$$\Delta G_{c-a} = \Delta g_{c-a} \cdot \frac{4}{3}\pi r^3 - \left(P\varepsilon_v + \tau_{\max}\gamma\right) \cdot \frac{4}{3}\pi r^3 + \gamma_{c/a} \cdot 4\pi r^2 \quad (1)$$

where ΔG_{c-a} is the energy gain of nucleating a spherical amorphous nucleus, Δg_{c-a} =14.2 kJ/mol (28) and $\gamma_{c/a}$ =0.08 J/m^2 (28) are the volumetric Gibbs free energy barrier and crystalline/amorphous interfacial energy, respectively. ε_v and $\gamma \approx \varepsilon_v \left(1 + w_{spacing} / w_{band}\right)$ are the volumetric and localized shear strain, which can be obtained from the Ge shock-Hugoniot data (29). The second term on the right-hand side of Eq. 2 represents the work done by pressure and shear, which help to overcome the energy barrier and interfacial energy gain of nucleating an amorphous embryo. Such an effect is plotted in Fig. 4A. The monotonically increasing energy curve for zero-stress state (blue) indicates the difficulty of forming amorphous phase at ambient state whereas under shock, the curves (red and yellow) are convex and exhibit a critical condition $dG_{c-a}/dr = 0$, corresponding to the critical nucleus size of $r_c = 2\gamma_{c-a} / \left(P\varepsilon_v + \tau_{\max}\gamma - \Delta g_{c-a}\right)$.

Shock-generated heat is another important factor in amorphization and subsequent nanocrystallization: (1) the temperature rise at the shock front reduces the energy barrier of crystalline-to-amorphous transition; (2) upon further heat transfer, the newly formed amorphous structure can re-transform into energetically more favorable crystalline phase; (3) if the temperature is sufficiently high, shock-induced melting may occur; (4) the transient nature of the shock-induced thermal flux results in a self-quenching mechanism which leads to a hierarchical nanostructure.

The increase in temperature due to shock compression can be evaluated by considering both the homogeneous temperature rise (ΔT_{homo}) resulting from work done by hydrostatic pressure and localized temperature rise (ΔT_{local}) resulting from work done by shear stress. The latter

assumes a balance between relaxation of deviatoric strain energy and increase in internal energy with heat loss to its surroundings, and thus gives a rough estimate of the temperature inside the amorphous band (19):

$$\begin{aligned} T_{band} &= T_0 + \Delta T_{homo} + \Delta T_{local} \\ &= T_0 + \frac{P\Delta V}{C_p} + \frac{2\dot{Q}w_{band}}{\sqrt{\pi}} \cdot \sqrt{\frac{t}{k\rho C_p}} \end{aligned} \quad (2)$$

where T_0 is the pre-shock temperature, ΔV is the volume change, $\dot{Q} \approx \beta\tau_{\max}\gamma/\Delta t$ is the rate of heat generation by converting deviatoric strain energy, β is the conversion efficiency (usually taken as 0.9), Δt ~1 ns is the duration of the laser pulse. k, ρ, C_p are the heat conductivity, density and heat capacity of the amorphous band, respectively. It should be noted that the shear stress is assumed to be independent of shock stress after the Hugoniot elastic limit (HEL~4 GPa for Ge (15)) as it is relaxed by plastic deformation. Fig. 4B shows the plot of shock-induced temperature together with melting temperature as a function of shock stress. The intersections of T_{homo} and T_{band} with T_m give the critical shock stresses (17.5 GPa for T_{homo} and 14 GPa for T_{band}) for the onset of amorphization. Clearly, the presence of shear stress lowers the threshold for amorphization. These calculations, whose accuracy depends largely on the material parameters, agree qualitatively with our experimental observations.

In summary, we have shown that germanium undergoes amorphization and nanocrystallization under extreme shock deformation. Although it is difficult, at this stage, to conclude whether these processes are solid-state or the result of melting and quenching, the presence of shear stress is definitely crucial, and enhances the understanding of pressure-induced amorphization and polyamorphisms (30–32). After its discovery in olivine (*20*), shock-induced directional amorphization has now been confirmed in Si (*18*) and B_4C (*19*), and hence should be

considered as a new deformation mechanism in this extreme regime. More practically, our results suggest high-power, pulsed laser as a new tool to quickly produce substrate-free, micrometer-scale, gradient nanostructured semiconductors.

References

1. Lu L, Shen Y, Chen X, Qian L, Lu K (2004) Ultrahigh strength and high electrical conductivity in copper. *Science* 304(5669):422–426.
2. Thevamaran R, et al. (2016) Dynamic creation and evolution of gradient nanostructure in single-crystal metallic microcubes. *Science* 354(6310):312–316.
3. Thompson M, Galvin G, Mayer J (1984) Melting temperature and explosive crystallization of amorphous silicon during pulsed laser irradiation. *Phys Rev Lett* 52(26):2360–2364.
4. Zhong L, Wang J, Sheng H, Zhang Z, Mao SX (2014) Formation of monatomic metallic glasses through ultrafast liquid quenching. *Nature* 512(7513):177–180.
5. Sharma SM, Sikka SKK (1996) Pressure induced amorphization of materials. *Prog Mater Sci* 40(1):1–77.
6. Machon D, Meersman F, Wilding MC, Wilson M, McMillan PF (2014) Pressure-induced amorphization and polyamorphism: Inorganic and biochemical systems. *Prog Mater Sci* 61(December 2013):216–282.
7. Mishima O, Calvert LD, Whalley E (1984) "Melting ice" I at 77 K and 10 kbar: a new method of making amorphous solids. *Nature* 310(5976):393–395.
8. Deb SK, Wilding M, Somayazulu M, McMillan PF (2001) Pressure-induced amorphization and an amorphous-amorphous transition in densified porous silicon. *Nature* 414(6863):528–30.
9. Grocholski B, Speziale S, Jeanloz R (2010) Equation of state, phase stability, and amorphization of SnI4 at high pressure and temperature. *Phys Rev B* 81(94101):1–7.
10. Nesterenko VF (1984) Scope for producing supercooled melts by a dynamic method. *Combust Explos Shock Waves* 19(5):665–667.
11. Jamieson JC (1963) Crystal Structures at High Pressures of Metallic Modifications of Silicon and Germanium. *Science* 139(3556):762–764.
12. Oliver DJ, Bradby JE, Williams JS, Swain M V., Munroe P (2009) Rate-dependent phase transformations in nanoindented germanium. *J Appl Phys* 105(12):40–43.
13. Pavlovskii MN (1967) Formation of metallic modification of Germanium and Silicon

under shock loading. *SovPhysSolidState* 9:2514--2518.

14. Graham RA, Jones OE, Holland JR (1966) Physical behavior of germanium under shock wave compression. *Solid State Commun* 27(5):1519–1529.

15. Gust WH, Royce EB (1972) Axial yield strengths and phase-transition stresses for 〈100〉, 〈110〉, and 〈111〉 germanium. *J Appl Phys* 43(11):4437–4442.

16. Clarke D, Kroll M, Kirchner P, Cook R, Hockey B (1988) Amorphization and Conductivity of Silicon and Germanium Induced by Indentation. *Phys Rev Lett* 60(21):2156–2159.

17. Gamero-Castaño M, Torrents A, Borrajo-Pelaez R, Zheng J-G (2014) Amorphization of hard crystalline materials by electrosprayed nanodroplet impact. *J Appl Phys* 116(17):174309.

18. Zhao S, et al. (2015) Pressure and shear induced amorphization of silicon. *Extrem Mech Lett* 5:74–80.

19. Zhao S, et al. (2016) Directional amorphization of boron carbide subjected to laser shock compression. *Proc Natl Acad Sci* (21):201604613.

20. Jeanloz R, et al. (1977) Shock-Produced Olivine Glass : First Observation. *Science* 197(4302):457–459.

21. Levitas VI, Ravelo R (2012) Virtual melting as a new mechanism of stress relaxation under high strain rate loading. *Proc Natl Acad Sci U S A* 109(33):13204–7.

22. Levitas VI (2005) Crystal-amorphous and crystal-crystal phase transformations via virtual melting. *Phys Rev Lett* 95(7). doi:10.1103/PhysRevLett.95.075701.

23. Tersoff J (1988) Empirical interatomic potential for silicon with improved elastic properties. *Phys Rev B* 38(14):9902–9905.

24. Plimpton S (1995) Fast Parallel Algorithms for Short-Range Molecular Dynamics. *J Comput Phys* 117(1):1–19.

25. Gumbsch P, Gao H (1999) Dislocations Faster than the Speed of Sound. *Science* 283(5404):965–968.

26. Jayaraman A, Klement JR W, Kennedy GC (1963) Melting and polymorphism at high pressures in some group IV elements and III-V compounds with the diamond/zincblende structure. *Phys Rev* 130:540–547.

27. Zhao S, et al. (2016) Amorphization and nanocrystallization of silicon under shock compression. *Acta Mater* 103:519–533.

28. Sandoval L, Reina C, Marian J (2015) Formation of Nanotwin Networks during High-Temperature Crystallization of Amorphous Germanium. *Sci Rep* 5(August):17251.

29. McQueen RG, Marsh SP (1970) The equation of state of solids from shock wave studies.

High Velocity Impact Phenomena, ed Kinslow R (Academic Press, New York), pp 293–417, 521–568.

30. McMillan PF, Wilson M, Daisenberger D, Machon D (2005) A density-driven phase transition between semiconducting and metallic polyamorphs of silicon. *Nat Mater* 4(9):680–4.

31. Corsini N, et al. (2015) Pressure-induced amorphisation and a new high density amorphous metallic phase in matrix-free Ge nanoparticles. *Nano Lett*:151012140302005.

32. McMillan PF (2002) New materials from high-pressure experiments. *Nat Mater* 1(1):19–25.

Acknowledgement This research is funded by a UC Research Laboratories Grant (09-LR-06-118456-MEYM) and a National Nuclear Security Administration (NNSA) Grant (DE-NA0002930). We acknowledge the highly professional support team of the Omega laser facility in the Laboratory of Laser Energetics, University of Rochester. B.R. and C.W. also wish to acknowledge the support of a US. Department of Energy grant (DE-AC52-07NA27344). Electron microscopy was conducted at CNMS User Facility, Oak Ridge National Laboratory, which is sponsored by the Office of Basic Energy Science, US. Department of Energy. The enthusiastic help by Dorothy Coffey is deeply acknowledged.

Figures and Captions

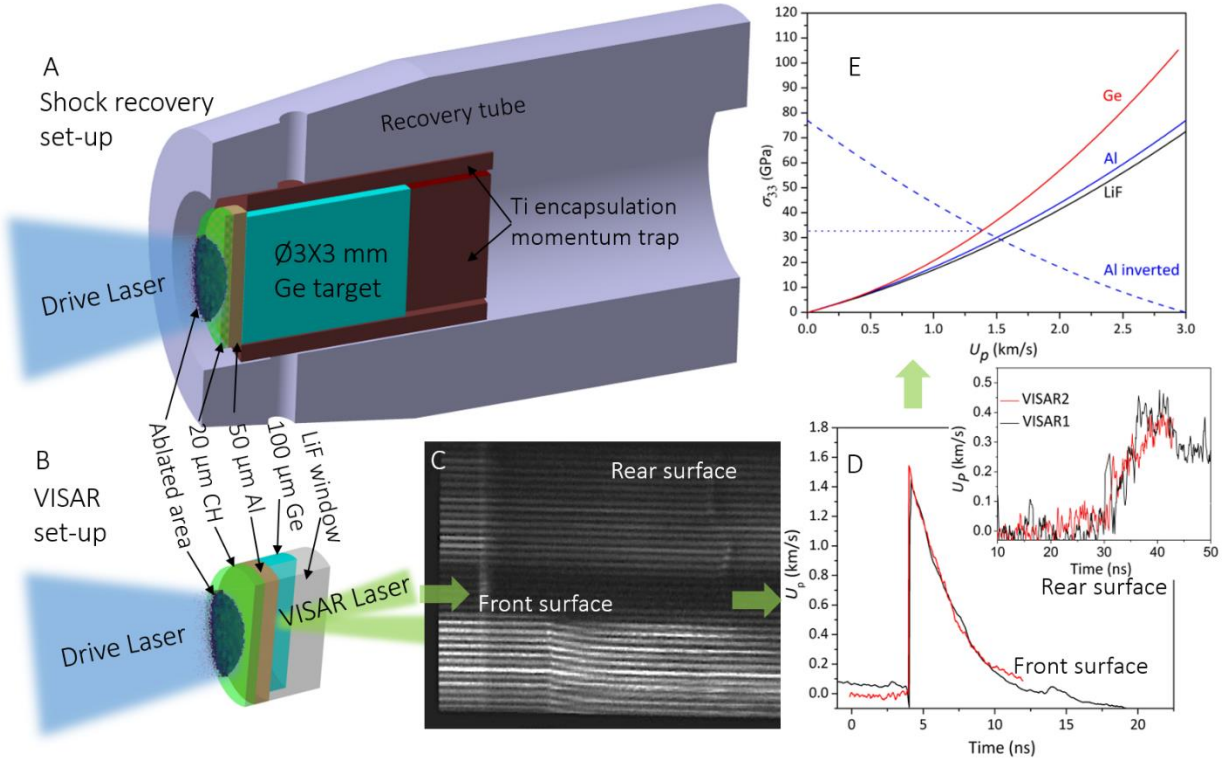

Figure 1 Laser-driven, shock-recovery experimental set-up, velocimetry measurement, and determination of shock stresses: (A) shock-recovery assembly with target package (along the laser path: 20 µm CH ablator, 50 µm Al pusher and Ø3 X 3mm Ge crystal) encapsulated in Ti and backed by momentum trap (Ti). The assembly is mounted in a recovery tube; (B) VISAR target package is similar to that of the recovery experiment except that a 100 µm thick half-cylindrical Ge foil is used so as to capture the information from both front (Al/LiF) and rare (Ge/LiF) surface of the target. The laser-transparent LiF window is glued to the rear surfaces of Ge target on one side and Al pusher on another side; (C) Temporally resolved VISAR fringes showing the shock break-out at front and rare surfaces of the sample. (D) Measured particle velocity, U_p as a function of time. (E) Determination of the peak shock stress on the front surface of Ge target by impedance matching. Note that Al and LiF are closely impedance-matched in the regime involved in our study.

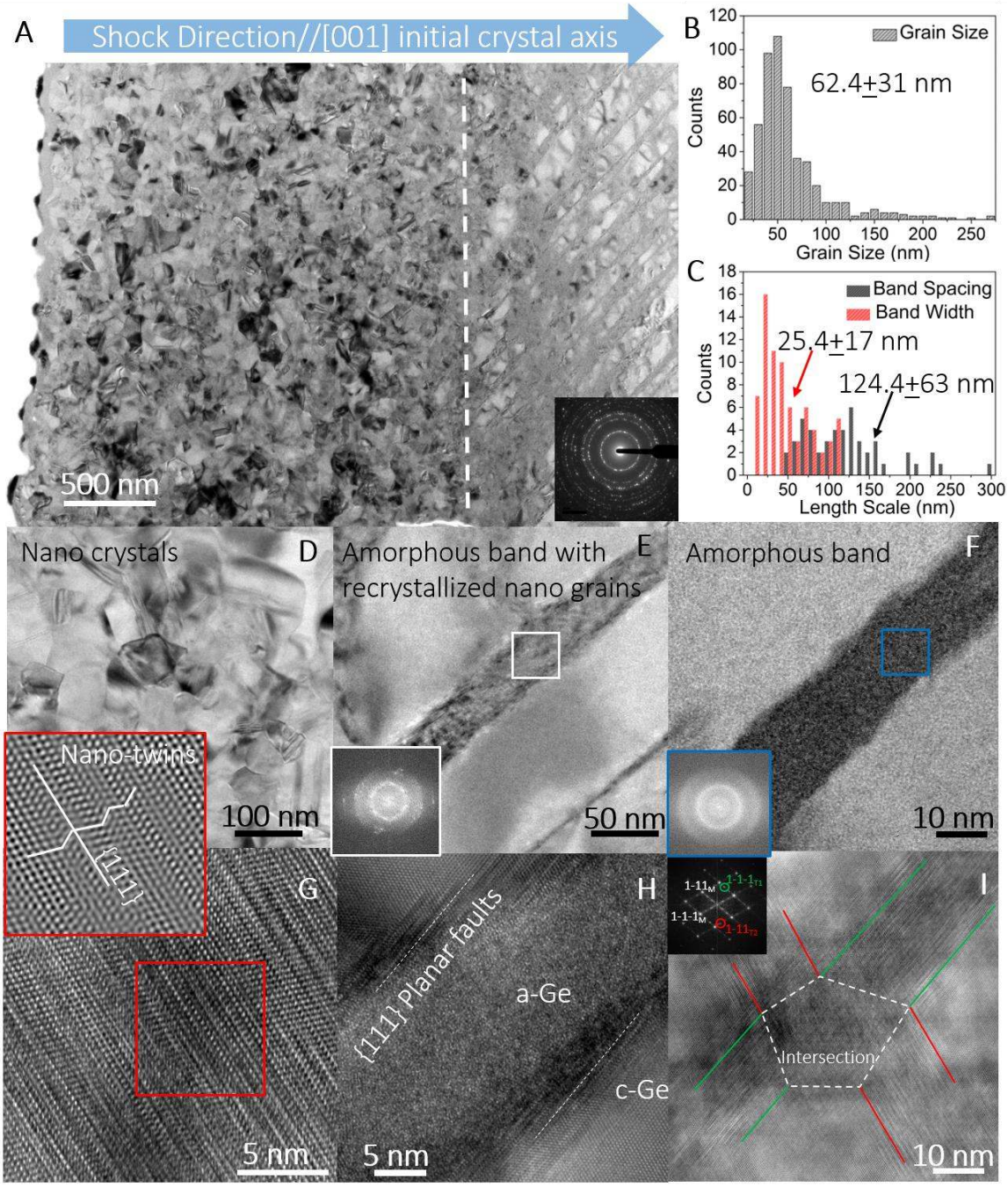

Figure 2 TEM/HRTEM micrographs of laser-shock recovered germanium: (A) TEM image shows the hierarchy of the deformation microstructure. (B) Distribution of the grain size in the nanocrystalline domain and (C) amorphous band width and spacing. (D) Zoomed view of nanocrystal. (E) Zoomed view of partially amorphous band with embedded nano-crystals. (F) Zoomed view of a completely amorphous band showing zero contrast inside the band. The corresponding Fourier-transformed diffractions in the boxed regions are shown in the insets. (G) Lattice image in a nanocrystal shows nano-scale twins/stacking faults on {111} planes. The Fourier-filtered image in the red inset reveals the zigzag feature of these planar defects. (H) Amorphous band with stacking faults in its vicinity. (I) Two {111} stacking fault packets intersect, resulting in the early stage of amorphization and two set of twin spots on the diffraction pattern.

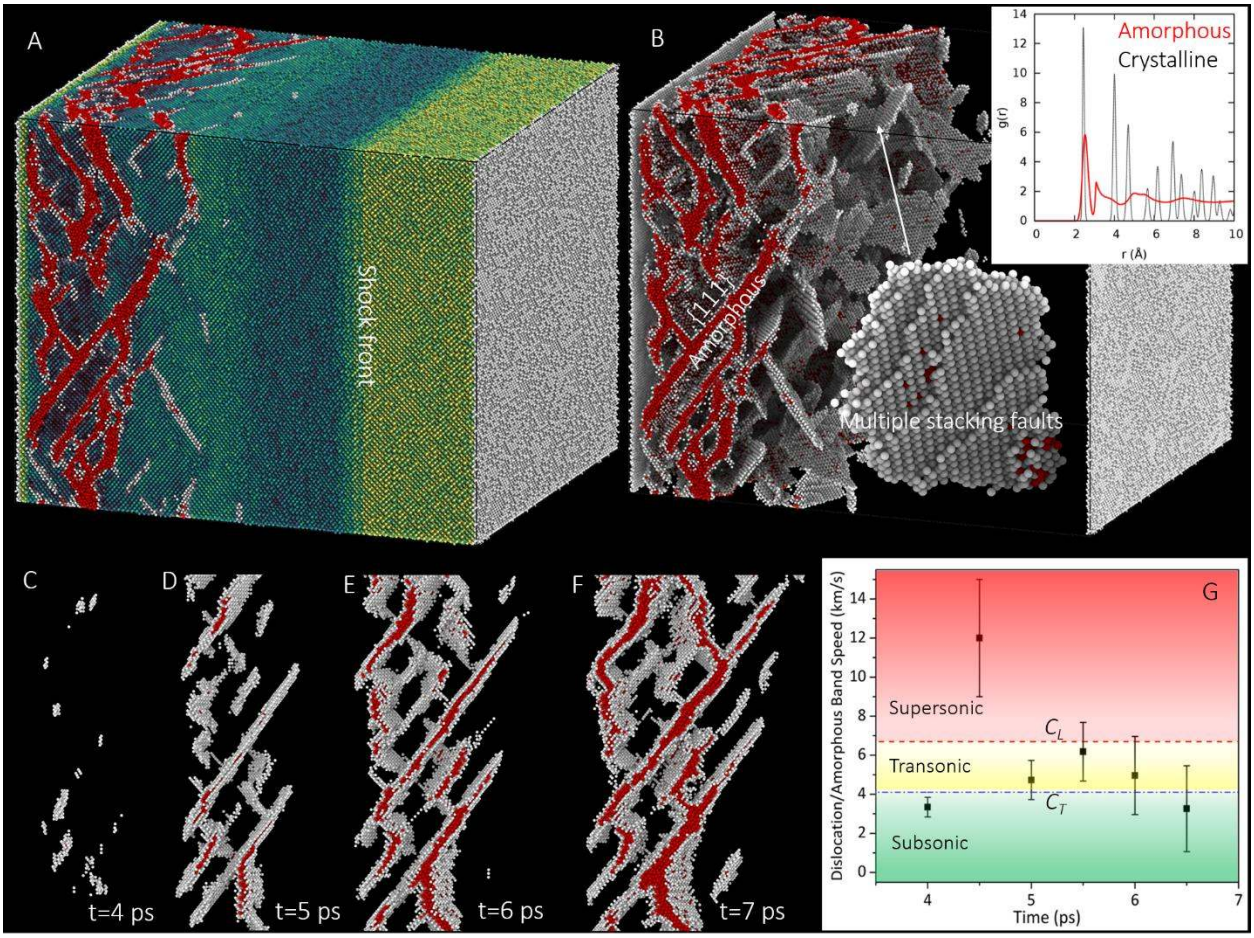

Figure 3 Molecular dynamics simulation of partial dislocation propagation and amorphization: (A) 3-D visualization of shocked germanium colored by coordination number. The amorphous bands are colored red. (B) Only the plastically-deformed (defected) atoms are shown, suggesting that the amorphous bands are preceded by partial dislocations (stacking faults). The amorphous band aligns roughly with {111} slip plane. Radial pair distribution functions (inset) distinguish the amorphous domain from crystalline structure. (C-F) Four snapshots showing the evolution of stacking faults and then amorphous bands. (G) Measurement of dislocation/amorphous band speed during shock compression and supersonic burst of dislocation is notified prior to the formation of amorphous band.

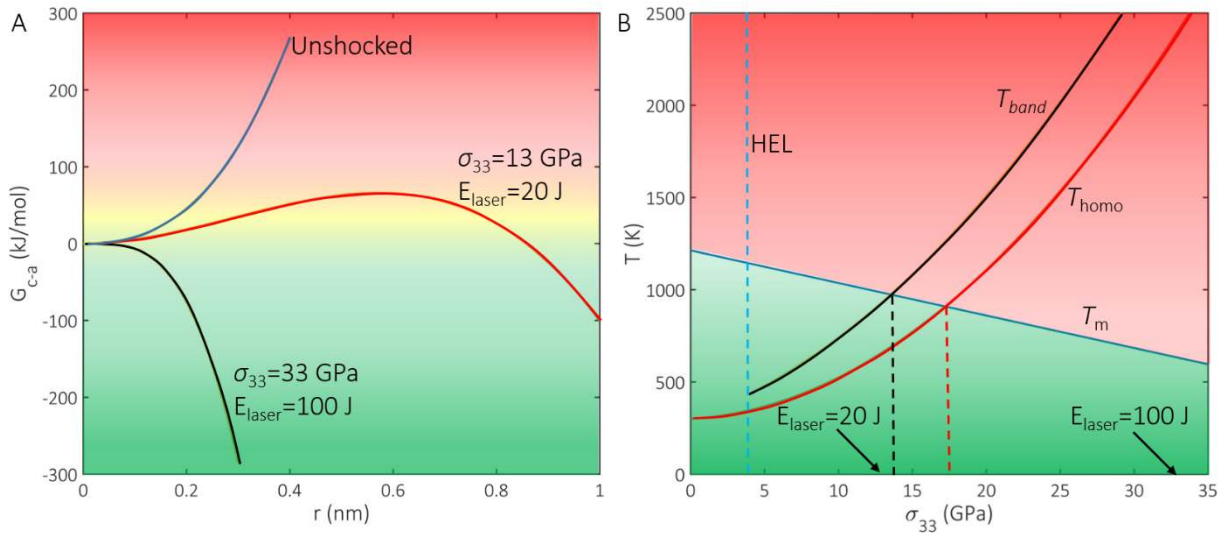

Figure 4 Thermodynamic analysis of amorphization: (A) Gibbs free energy change associated with nucleation of an amorphous embryo. The presence of shock stress (pressure plus shear) renders it possible to overcome the energy barrier of crystalline-to-amorphous transformation; (B) Pressure-induced homogeneous temperature (T_{homo}) and shear-induced localized temperature (T_{local}) compared with the decreasing melting temperature (T_m) as a function of shock stress (negative Clapeyron slope). The intersections represent the critical shock stresses of crystalline-to-amorphous transition, indicating that shear stress lower the threshold.

Supporting Information for

Generating Gradient Germanium Nanostructures by Shock-induced Amorphization and Crystallization

S. Zhao[a], B. Kad[a], C.E. Wehrenberg[b] , B.A. Remington[b], E.N. Hahn[a], K. More[c], M.A. Meyers[a*]

[*]Corresponding author. Email: mameyers@eng.ucsd.edu (M.A.M)

This PDF file includes:

Materials and Methods

Supplementary Text

Figs.S1- S4

Captions for Movie S1

References

Other Supplementary Material for this manuscript includes the following:

Movie S1

Materials and Methods

Laser shock recovery experiments

We performed laser-driven shock-recovery experiments at Omega laser facility, Laboratory of Laser Energetics, University of Rochester. The shock wave is created by the following sequence of processes. First, the high power pulsed laser energy is deposited on the 20 um CH ablator of the target package, ionizing it into plasma. Second, as the plasma flows away, the target surface experiences a reaction force equal to the rate at which momentum is carried away due to the rocket effect. The stress pulse promptly builds up and transforms into a shock wave. Third, the shock wave propagates inwards and quickly decays as the laser duration is very short (1ns). The amplitude of the ablation pressure (P_{abl}) can be estimated by the analytical model put forward by Lindl (*33*),

$$P_{abl} = C\left(\frac{I}{\lambda}\right)^{\beta} \tag{1}$$

where C is a material-dependent constant and λ is the wavelength of the laser. $I = \frac{E_{laser}}{At}$ is the laser irradiance and β is the material-dependent exponential (calibrated to be 0.71 for diamond (*34*), which is similar to our CH ablator). The target package consists of a 20 µm CH ablator, 50 µm Al foil, Ø 3X3 mm cylindrical Ge target and Ti momentum trap. The assembly is encapsulated within a Ti cup. The Al foil has two functions: (1) as a heat shield to minimize the preheating induced by laser irradiation and (2) as a pulse shaper to render the shock pulse on the target surface planar (uniaxial strain state). The laser pulse is nominally a 1ns square pulse of 351 nm (3 omega) laser light. The beam was used without phase plates and defocused to a spot size of 3 mm diameter.

VISAR analysis and impedance matching

Separate VISAR experiments were conducted to measure the particle velocity and further infer the shock pressure. A 532 nm probe laser is reflected from the rear surface of the moving target and then it will pass through collection optics and be routed into two separate streak cameras. Each of them uses a different etalon thickness. The VISAR target is comprised of a 20 µm CH ablator, 50 µm Al foil, a half-moon Ge sample (100 µm thick) and laser-transparent LiF window. This specific geometry of the target allows the measurement of particle velocity of both front and rear surface of the Ge sample, which shows the rapid decay of the shock pressure as function of the depth. A correction factor of 0.775 is applied to the apparent velocity to account for the pressure dependence of the index of refraction of the LiF window. Conservation of mass and momentum give the relationship between the initial density ρ_0 particle velocity U_p, shock velocity U_s and shock stress σ_{33},

$$\sigma_{33} \approx \rho_0 U_s U_p \quad (2)$$

where $\rho_0 U_s$ is often termed as shock impedance, which can be obtained from the slope of the shock Hugoniot curves (σ_{33} vs. Up) in Fig. 1E of the main text. At the interface between the Al foil and Ge sample, shock wave is reflected and the shock stress changes. The inverted shock Hugoniot of Al (red dotted line in Fig. 1E) gives the estimate of the reflected shock wave and the intersection of this line with Ge curve (black line in Fig. 1E) yield the shock pressure on the front surface of the Ge sample. Such a process is termed as impedance matching (*35*). The shock stress at the rear surface of Ge sample can be read directly from the Ge Hugoniot curve.

Radiation-hydrodynamic simulations

Radiation-hydrodynamics simulations were performed using the HYADES code to aid in the design of the experiment and interpretation of the results. The target was modeled as a 1-D stack consisting of 20 μm polystyrene ablator, 3 μm of glue (approximated as polystyrene), 50 μm Al, 3 μm glue (polystyrene), and 125 μm Ge. In order to simulate VISAR data, an additional layer of glue and LiF were substituted at the corresponding interface (front or back of the Ge). A rate-independent Steinberg-Guinan model was used to model the strength of Al (*36*). The Ge was modeled as elastic-perfectly plastic using the Von Mises yield criterion with Y_{VM} = 4 GPa, consistent with observations of the Ge Hugoniot elastic limit.

TEM sample preparation and observation

Transmission electron microscopy is the ultimate tool to characterize the postmortem microstructure of the shocked target. To prepare TEM samples cite-specifically, a Hitachi NB5000 scanning electron microscope (SEM) equipped with a focus ion beam (FIB) was used to cut TEM samples directly from the laser-shocked germanium monocrystal surface. The TEM foils were ion milled by 30 kV Ga beam and finally polished at 5kV to minimize FIB damage. The as-lifted sample is shown in the SEM image in Fig. S1B. A Hitachi HF3300 transmission electron microscope operated at 300 keV was employed to characterize the post-shock microstructure. In addition to the results shown in the main text (Fig. 2) where the Ge target was laser shocked with a high energy (E_{laser}=100 J, σ_{33}~33 GPa), Fig. S1C shows the microstructure of the Ge target shocked at a low energy (E_{laser}=20 J, σ_{33}~10 GPa). The contrast-less feature of the high resolution TEM image suggest the random arrangement of the atoms. The Fourier-transformed diffractograph exhibits a halo-shaped ring pattern, confirming the amorphous nature of the materials.

Molecular dynamics simulations

Molecular dynamics simulations of shocked Ge were conducted using LAMMPS utilizing the Tersoff potential under NVE conditions. Shock compression was conducted along the [001] direction in single crystalline germanium using a non-equilibrium drive piston. The piston was linearly accelerated to 1.2 km/s over 1 ps and held constant for the duration of the simulation. The system employs periodic boundaries perpendicular to the shock direction to create a uniaxial strain state. The lateral dimensions are 40 nm and the dimension along the direction of shock wave propagation is 50 nm to the rear surface. In order to compare the simulation to the experiments where the wave decays fully as it traverses the sample, analysis is only conducted prior to the reflection of the shock wave from the rear surface. The imparted particle velocity, U_p = 1.2 km/s, generates a shock pressure of 40.5 GPa and a concomitant deviatoric shear stress

of 10.5 GPa. The corresponding shock speed, U_s = 5.2 km/s. Analysis of the shock-induced defect structure is completed using the "Identify Diamond Structure" implemented within OVITO (*37*). In order to successfully apply this analysis technique to a strained lattice, an affine scale is first applied to artificially revert the strain such that analysis correctly identifies the defects. If this step is not completed the analysis tool identifies the uniaxially compressed region as unidentified non-dc atoms. Upon successful analysis, an affine scale exactly opposite in magnitude is applied to perfectly return the atoms to their original positions. Further analysis is conducted of the pair distribution function (*38*) on the crystalline and amorphous regions. It describes the probability, g(r), of finding an atom at a given distance, r, away from any other atom. The shape and peaks of the curve can be used to differentiate between phases and can also provide coordination information.

Supplementary Text:

Shear Stresses under Shock Compression

The shock stress (σ_{33}), hydrostatic pressure (P) and maximum shear stress (τ_{max}) can be obtained from the generalized Hooke's law for uniaxial strain, $\sigma_{ij} = C_{ij33}\varepsilon_{33}$ where C_{ijkl} is the elastic constants and ε_{33} is the uniaxial strain and x_3 is the direction of shock wave propagation. The ratio $\tau_{\max} / P$ can be expressed as a function of elastic stiffness (if the deformation is assumed to be purely elastic) as,

$$\frac{\tau_{\max}}{P} = \frac{3\left(C_{11} - C_{12}\right)}{2\left(C_{11} + 2C_{12}\right)} \qquad \text{S.1}$$

For germanium, at ambient pressure, C_{11}= 129.2 GPa, C_{12}=47.9 GPa, rendering $\tau_{\max} / P \approx 0.54$. This is a first approximation since the elastic moduli are pressure-dependent as predicted by our MD simulations (Fig. S3 in **SM**). This high shear stress is relaxed by directional deformation and subsequent amorphous band formation.

Supersonic Dislocation

Both our TEM observations and MD simulations show that dislocation (stacking faults) activity occurs prior to the amorphization, suggesting that dislocations are the trigger to the drastic crystalline-to-amorphous transition. Therefore, it is reasonable to infer that the kinetics of dislocation motion determine the kinetics of amorphization. It has been predicated by the theory of linear elasticity that the dislocation velocity is limited by the transverse wave speed (C_T) at which the energy associated with the screw dislocation approaches infinity, as shown in Eq. 3.

$$\frac{W}{l} = \frac{Gb^2}{4\pi\left(1-\frac{{v_d}^2}{{C_T}^2}\right)^{1/2}} \ln\frac{R}{b} \qquad \text{S.2}$$

Where W is the elastic energy associated with a moving screw dislocation, l is the length and b is the Burgers vector. However, MD simulation by Gumbsch and Gao (*25*) suggested the existence of supersonic dislocation in tungsten, even above longitudinal sound speed. Gumbsch and Gao (25) proposed that a supersonic dislocation can be obtained if an ultrafast dislocation seed is nucleated at a stress concentrator. An applied stress is required to help the dislocation to overcome the sound barrier. Such a condition can be most-likely achieved in the strong shock experiment where the high stress state (both hydrodynamic and deviatoric components) build up quickly at the shock front. In our MD simulations, supersonic dislocation bursts are identified, as shown in Fig. 3, prior to amorphization. The motion of dislocation is non-uniform at this stage and the velocity should be a range instead of a constant. After such a supersonic event, the dislocation velocity quickly falls off when the amorphization is initiated and the motion of dislocation/amorphous band is transonic and uniform. The supplementary video and MD snapshots in Fig. 3 show how the partial dislocations nucleate, catch up with the shock front, and eventually give rise to the formation of amorphous bands.

Estimation of Sound Speeds and Dislocation Velocity

Travel of acoustic waves in crystal is highly anisotropic and orientation dependent. Germanium is a cubic material and the active slip system is of {111}<110> type. Thus, we need to evaluate the sound speeds along <110> direction to compare them with the dislocation velocity. The corresponding longitudinal sound speed is:

$$C_L = \left(\frac{C_{11}+C_{12}+2C_{44}}{2\rho}\right)^{1/2} \qquad \text{S.3}$$

The transversal sound speed is polarized in different <110> directions:

$$C_{T\max} = \left(\frac{C_{44}}{\rho}\right)^{1/2}$$
$$C_{T\min} = \left(\frac{C_{11}-C_{12}}{2\rho}\right)^{1/2} \qquad \text{S.4}$$

It should be noted that the elastic constants C_{11}, C_{12}, C_{44} are a function of pressure, as shown in Fig. S3A. Thus, the sound speeds also depend on pressure, which are plotted in Fig. S4.

Dislocation velocity (V_d) is estimated by tracking the displacement of the defects in time. Multiple snapshots with 1 ps spacing (in MD time) are used and the effective defect length is measured from each snapshot. It should be noted that the motion/growth of these defects are not strictly limited in one particular direction and we also notice the lateral growth of the stacking faults/amorphous bands, suggesting the activation of stacking faults in the adjacent slip planes. Due to these complexities, the defect velocity was measured several times to minimize the errors caused by the uncertainty of the defect length. Despite of the error bars, our measurements in Fig. 4G of the main text show that the partial dislocations nucleate with an ultrafast velocity ($V_d \sim C_T$) right after the shock front passed by. Shortly after their nucleation, the dislocations are still under extremely high stresses and they quickly accelerate to the supersonic ($V_d > C_L$) regime. However, the motion of supersonic dislocations is not steady state, i.e. the velocity should be a range instead of a number. After such an explosive motion/growth, their velocity falls to the transonic regime ($C_L > V_d > C_T$). The supersonic dislocations seem to trigger the amorphization which helps to relax the concentrated deviatoric stress.

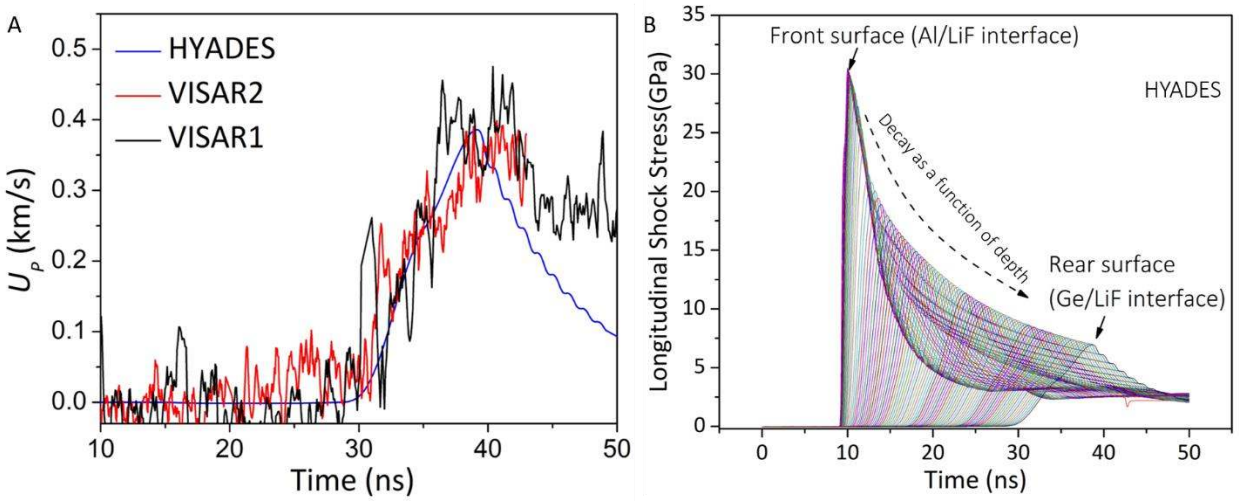

Figure S5 HYADES simulation of shock-wave propagation and decay in Ge: (A) Calibration of the simulation with the experimentally-determined velocity profile at the Ge/LiF interface (rear surface); (B) simulated longitudinal shock stress vs. time profile at different depths below the shock surface, showing the decay of the amplitude of the stress wave as it passes through the material.

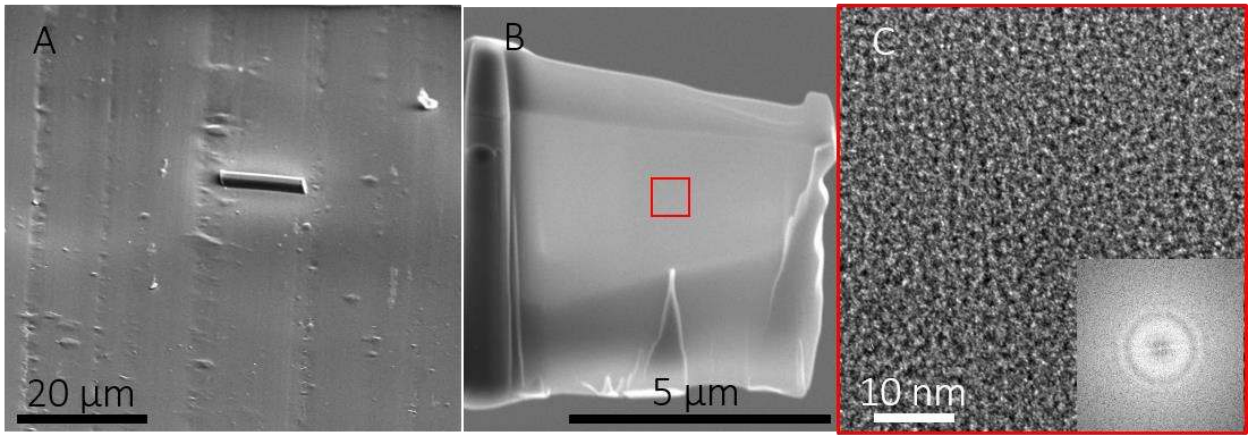

Figure S6 Micrographs of Ge shocked at a lower laser energy (20 J): (A) scanning electron microscopy image of the shocked surface of [001] Ge single crystal. The rectangle indicates the position of the TEM sample cut by focused ion beam technique; (B) SEM image of the TEM sample cross-section; (C) High resolution TEM image shows that the deformed structure is indeed amorphous without long-range order. The amorphous feature can be also confirmed by fast-Fourier transformed diffractography in the bottom-left corner.

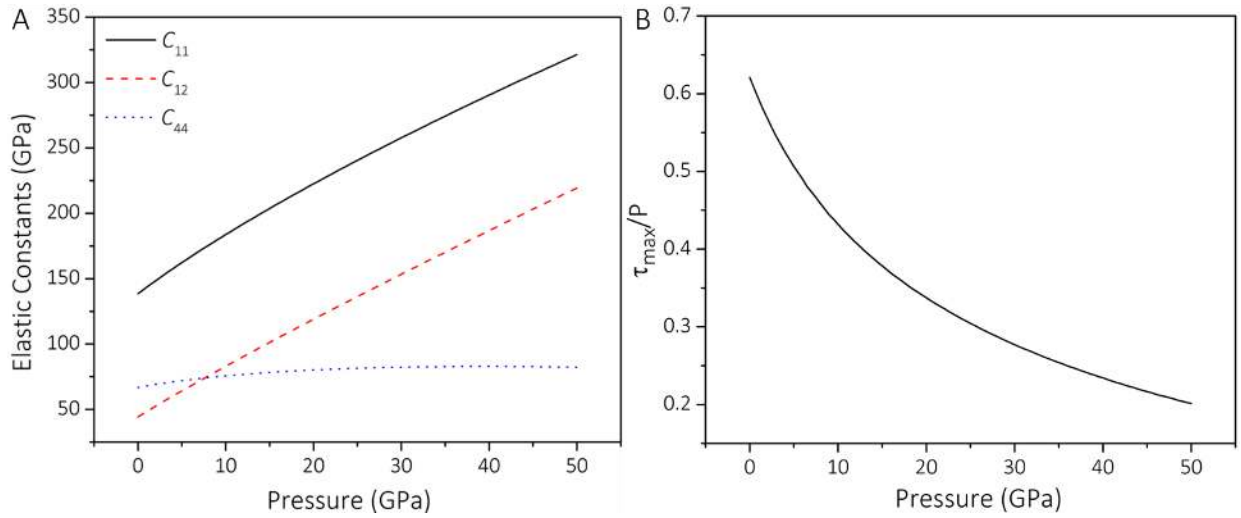

Figure S7 (A) MD prediction of pressure dependency of elastic constant and (B) ratio of maximum shear over pressure (assuming elasticity and no relaxation).

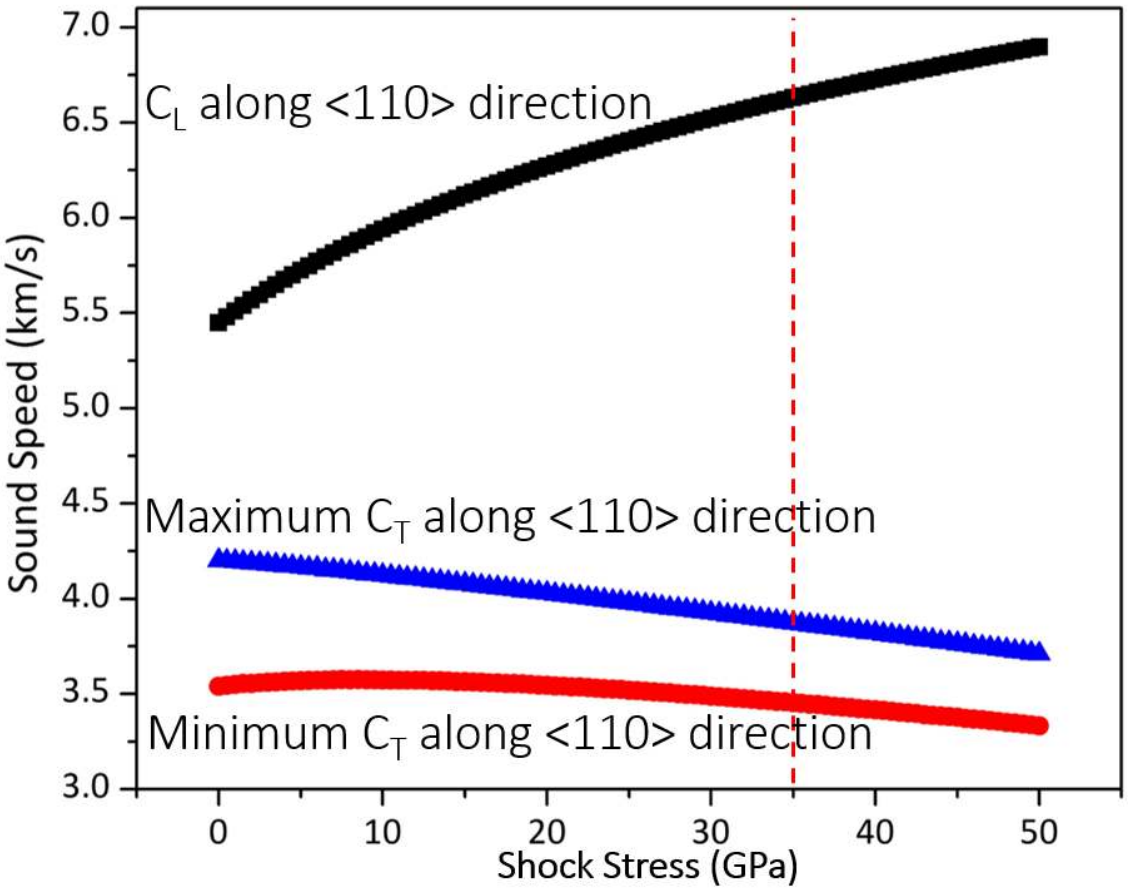

Figure S8 Pressure dependency of longitudinal sound speed, transverse sound speed (split into two different values due to crystal anisotropy) along <110> slip direction. The intersection of the vertical red dotted line with the black line gives the longitudinal sound speed at the pressure matched with the condition of the MD simulation (roughly agree with experiment as well).

Captions for the supplementary movie:

The movie of MD simulation snapshots captures the process of shock-induced amorphization: left panel, 3-D view of the entire simulation box; right panel, (110) projection in the vicinity of the transformation regime. The movie is colored by von Mises Stress (GPa). Directional amorphization occurs after the passage of the shock front.

Additional References

33. J. Lindl, Development of the indirect-drive approach to inertial confinement fusion and the target physics basis for ignition and gain. *Phys. Plasmas*. **2**, 3933 (1995).

34. D. E. Fratanduono *et al.*, Refractive index of lithium fluoride ramp compressed to 800 GPa. *J. Appl. Phys.* **109** (2011), doi:10.1063/1.3599884.

35. M. A. Meyers, *Dynamic behavior of materials* (John Wiley & Sons, 1994).

36. D. J. Steinberg, S. G. Cochran, M. W. Guinan, A constitutive model for metals applicable at highstrain rate. **1498** (1980), doi:10.1063/1.327799.

37. A. Stukowski, Visualization and analysis of atomistic simulation data with OVITO–the Open Visualization Tool. *Model. Simul. Mater. Sci. Eng.* **18**, 15012 (2010).

38. B. G. Levine, J. E. Stone, A. Kohlmeyer, Fast Analysis of Molecular Dynamics Trajectories with Graphics Processing Units—Radial Distribution Function Histogramming. *J. Comput.* **230**, 3556–3569 (2011).